SiO$_2$-bearing Fluxes Induced Evolution of γ Columnar Grain Size

Compositional dependence of γ columnar grain size upon submerged arc welding fluxes for EH36 shipbuilding steel is demonstrated

BY C. HAN, M. ZHONG, P. ZUO, AND C. WANG

Abstract

Understanding the controlling mechanisms of γ columnar grain size in the weld metal of low-carbon, low-alloy steel is critical for optimizing resultant microstructures and the weld metal's ensuing properties. Here, we investigate the role of welding flux composition upon the γ columnar grain size by submerged arc welding of EH36 shipbuilding steel with designed CaF$_2$-SiO$_2$ fluxes. We found that the addition of SiO$_2$ from 5 to 40 mass-% increases average columnar grain size by a factor of nearly 2.5, which results from the change of the weld pool solidification mode from peritectic to primary δ solidification. Such a change is directly related to element transfer behaviors between the flux and the weld metal. Furthermore, we offer compelling evidence that alterations in γ columnar grain size are not primarily governed by significantly populated inclusions and/or weld metal macro-morphological changes. Our findings may largely serve as a viable strategy toward designing welding consumables to match base metals to ensure the soundness of the weldment.

Keywords

- Submerged Arc Welding
- Flux
- Weld Metal
- γ Columnar Grain
- Peritectic Transition

Introduction

Solidification of the low-carbon, low-alloy steel weld metal (WM) generally starts with the primary solidification of δ-ferrite followed by the δ→γ phase transformation, finally ending with the formation of γ columnar grain (CG) structure (Refs. 1, 2). On further cooling, supercooled γ will decompose and transform into a microstructure composed of grain boundary ferrite, side plate ferrite, acicular ferrite, bainite, and even martensite (Refs. 1, 3). For low-carbon, low-alloy steel WMs, an acicular ferrite-dominated microstructure is one of the most sought-after scenarios for achieving optimal end-user properties (Ref. 4).

Mounting evidence has indicated that γ grain structure is critical in determining subsequent microstructural development during the cooling of the WM (Refs. 5–8). Bhadeshia et al. (Ref. 5) developed a model that demonstrated quantitative relationships between CG size and various microstructural contents. Farrar et al. (Ref. 6) reported that γ grain size influenced the γ→α transformation kinetics, thus altering microstructural morphologies and proportions of the γ decomposition products. Thewlis et al. (Refs. 7, 8) found that there was an intermediate range of γ grain size at which acicular ferrite formation was optimized. Therefore, to achieve a desirable microstructure in WMs, like acicular ferrite, optimizing the CG structure is necessary. The alloy content in WMs is acknowledged as a critical factor influencing the CG structure (Refs. 1, 3, 9–11). Bhadeshia (Ref. 3) suggested that alloy content might carry a significant effect on the CG structure, presumably by influencing the thermodynamics and kinetics of the δ→γ transformation. Evans (Ref. 9) reported that the CG size of the top weld beads decreased with the increase of C content in shielded metal arc welds from 0.044 to 0.150%. Zhang et al. (Ref. 1) found that CG size showed a trend of initially decreasing followed by an increase with the addition of Ni content. The minimum CG size was associated with an equivalent Ni content between 3.4 and 6.2 mass-%,

Table 1 — Chemical Compositions of Fluxes (Mass-%)

Flux No.	Designed		As-quenched	
	SiO_2	CaF_2	SiO_2	CaF_2
S-5	5	95	4.34 ($\pm$ 0.08)	95.66 ($\pm$ 0.16)
S-10	10	90	8.64 ($\pm$ 0.18)	91.36 ($\pm$ 0.27)
S-15	15	85	13.56 ($\pm$ 0.23)	86.44 ($\pm$ 0.34)
S-20	20	80	19.56 ($\pm$ 0.41)	80.44 ($\pm$ 0.37)
S-30	30	70	29.83 ($\pm$ 0.53)	70.17 ($\pm$ 0.54)
S-40	40	60	39.51 ($\pm$ 0.92)	60.49 ($\pm$ 0.85)

which was attributed to a peritectic transition when the WM solidified. O content (i.e., the inclusion content) is another factor that may contribute to variation in CG size, as finely dispersed inclusions have been proposed as pinning phases (Refs. 12–14) that could hinder the movement of the γ grain boundaries in WMs and reduce the γ grain size. Additionally, WM macromorphology may also exert a potential impact on CG development (Refs. 15, 16) because the profiles of the weld pool can significantly influence the cooling rates during the solidification, which may in turn affect CG growth.

During submerged arc welding (SAW), fluxes primarily consist of fluoride (CaF_2) and/or oxides (SiO_2, TiO_2, Al_2O_3, MnO, or even rare earth-type oxides), which may be subject to decomposition, driving chemical reactions at the slag-metal-gas interface. Such reactions can change O content and alloy levels in WMs (Refs. 17, 18). CaF_2 has been proven effective in modifying the slag melting point and viscosity (Ref. 18). SiO_2 is indispensably added to improve current capacity and slag detachability (Refs. 19, 20). Zhang et al. (Refs. 21, 22) have revealed that SiO_2 addition in the CaF_2-SiO_2 fluxes could greatly enhance Si and O transfer from the slag to the WM, which was accompanied by Mn loss and decarburization. In addition, a recent study showed that incorporating SiO_2 in the flux could significantly promote the inclusion volume fraction in WMs (Ref. 23).

Alterations in WM compositions or inclusions, influenced by flux composition, can modify pertinent solidification behaviors and subsequent δ→γ transformation and influence the resultant CG structure. However, as CGs are affected by multiple potential factors during their formation process, it is necessary to clarify the controlling mechanisms of the flux composition on CG size. To this end, we offered a new strategy to treat EH36 shipbuilding steel by a simple binary CaF_2–SiO_2 flux system and focused on the evolution of the CG size with the SiO_2 content in the fluxes. The controlling mechanism of the CG size through fine-tuned welding flux composition will be elaborated in detail. These findings may hold significant implications for flux optimization of welding technology toward fulfilling the promise of rational tailoring of composition, microstructure, and ultimate properties of targeted WMs.

Experimental

Flux Preparation

Fused binary CaF_2-SiO_2 fluxes were employed for the entire study. For suitable fusion flux (melting point generally 200°C lower than the base metal) (Ref. 24), SiO_2 was adjusted (5 to 40 mass-%) by referring to the CaF_2-SiO_2 phase diagram (Ref. 25). Fluxes were prepared from reagent-grade chemicals of CaF_2 (> 98.5 mass-%) and SiO_2 (> 99.7 mass-%) (all from Sinopharm Chemical Reagent Co. Ltd). For each flux, 1.0 kg powders were thoroughly mixed according to the target mass ratio shown in Table 1, in which the fluxes (also the WMs below) numbers represent corresponding nominal SiO_2 mass percentages. The numerical designation assigned to the WM indicates preparation from the corresponding flux number. To ensure homogeneity, each mixed reagent was pre-melted at 1550°C in a graphite crucible for 1 h. Subsequently, the pre-melted fluxes were quenched by cold water, and the collected fluxes were baked at 700°C for 2 h to remove moisture. Afterward, they were crushed and sieved to 8 to 40 mesh before SAW. Chemical compositions of the fluxes were confirmed by x-ray fluorescence (XRF, ZXS Priums II, Rigaku, Japan) and the ethylenediamine tetraacetic acid (EDTA) titration method, as shown in Table 1, where the as-quenched measurements show negligible differences compared with the corresponding designed values.

SAW Processing

Two types of EH36 shipbuilding steels with different C contents (well within the range dictated by ASTM A131, *Standard Specification for Structural Steel for Ships*) were selected, which were classified as low C (labeled as BM-L)

Table 2 — Chemical Compositions of Base Metals, Wire, and WMs (Mass-%)

Employed Materials	C	Si	Mn	Al	Ni	Cr	Mo	Ti	O
BM-L	0.075	0.195	1.26	0.035	0.362	0.124	0.061	0.016	0.0028
BM-H	0.175	0.260	1.44	0.060	0.010	0.020	0.006	0.010	0.0046
Wire	0.127	0.049	1.65	0.008	0.009	0.030	—	0.010	0.0030
WM-5	0.081	0.139	1.19	0.006	0.201	0.085	0.035	0.007	0.0169
WM-10	0.083	0.175	1.27	0.009	0.212	0.086	0.033	0.006	0.0185
WM-15	0.076	0.181	1.19	0.009	0.210	0.085	0.027	0.007	0.0211
WM-20	0.072	0.231	1.05	0.009	0.192	0.091	0.027	0.007	0.0240
WM-30	0.063	0.290	1.05	0.010	0.210	0.088	0.042	0.004	0.0335
WM-40	0.060	0.327	0.97	0.015	0.211	0.096	0.046	0.007	0.0397
WM-40H	0.124	0.364	1.07	0.017	0.015	0.096	0.004	0.006	0.0403

and high C (labeled as BM-H) steels, respectively. Bead-on-plate high heat-input SAW (Lincoln Electric Power Wave® AC/DC 1000 SD, Lincoln Electric, China) trials were performed on flat EH36 plates, 24 mm thick, in a single-pass manner. The welding parameters for the double-wire single-pass tandem SAW were DC-850A/32V for the forward electrode and AC-625A/36V for the backward electrode, respectively. A commercial electrode wire (CHWS3, Atlantic, China) with a diameter of 4 mm was used. The distance between the welding conductive nozzle and the steel plate was maintained at 25 mm, while the tip of the electrode wires measured an approximate distance of 15 mm from the steel plate before welding began. The spacing between the forward and backward electrode wires was 20 mm. The welding speed was maintained at 500 mm/min to achieve a heat input of 60 kJ/cm. Following the welding process, a weldment of approximately 30 cm in total length was attained, comprising a consistently uniform weld bead measuring around 15 cm.

Metallic elements in the base metals, electrode wire, and WMs were analyzed via inductively coupled plasma optical emission spectrometry (ICP-OES, Optima 8300, Perkin-Elmer). O (ONH836) and C (CS230) contents were determined using a LECO analyzer. Chemical compositions are given in Table 2, in which the WM samples from welding BM-L with six fluxes are labeled WM-5 to WM-40, and BM-H welded with S-40 is labeled WM-40H.

Metallographic Examination

For each WM, the specimens undergoing steady welding conditions were sectioned perpendicularly to the welding direction at three different locations 5 cm apart, and all three slices required metallographic examinations. These slices were prepared by standard metallographic procedures, which consist of mechanical grinding, mirror polishing by diamond suspensions up to 0.25 μm, and chemical etching by 4% nital. Subsequently, WM macromorphology was observed by a stereomicroscope (SZ61, Olympus, Japan). Corresponding quantifications (i.e., weld bead shape parameters, defined as the width (w), reinforcement height (H_r), penetration depth (D_p), fusion line length (L_f), area (S), and contact angle (θ), were measured from the macromorphology images using ImageJ software. CGs were assessed through graphical analysis using an optical microscope (OM, GX51, Olympus, Japan). The measurements utilized the linear intercept procedure, as recommended for anisotropic structures according to ASTM E112, *Standard Test Methods for Determining Average Grain Size* (Ref. 26). Each slice contained 36 fields of view at a magnification of 50× to cover the entire WM. Five test lines, normal to the major axes of CGs, were randomly placed to ensure that at least 50 intercepts were counted in each image. The term "CG size" in the current study refers to the "width" measured in a direction normal to the major axes of CGs on the transverse section of the WMs by the method described above.

Inclusion Examinations

The specimens for inclusion examinations were also cut transversely from the location undergoing steady welding conditions. Inclusion examinations were performed in the middle area of the mirror-polished specimens of the four WMs (WM-5, WM-20, WM-30, and WM-40). Inclusion size and quantity were identified at a magnification of 5000×
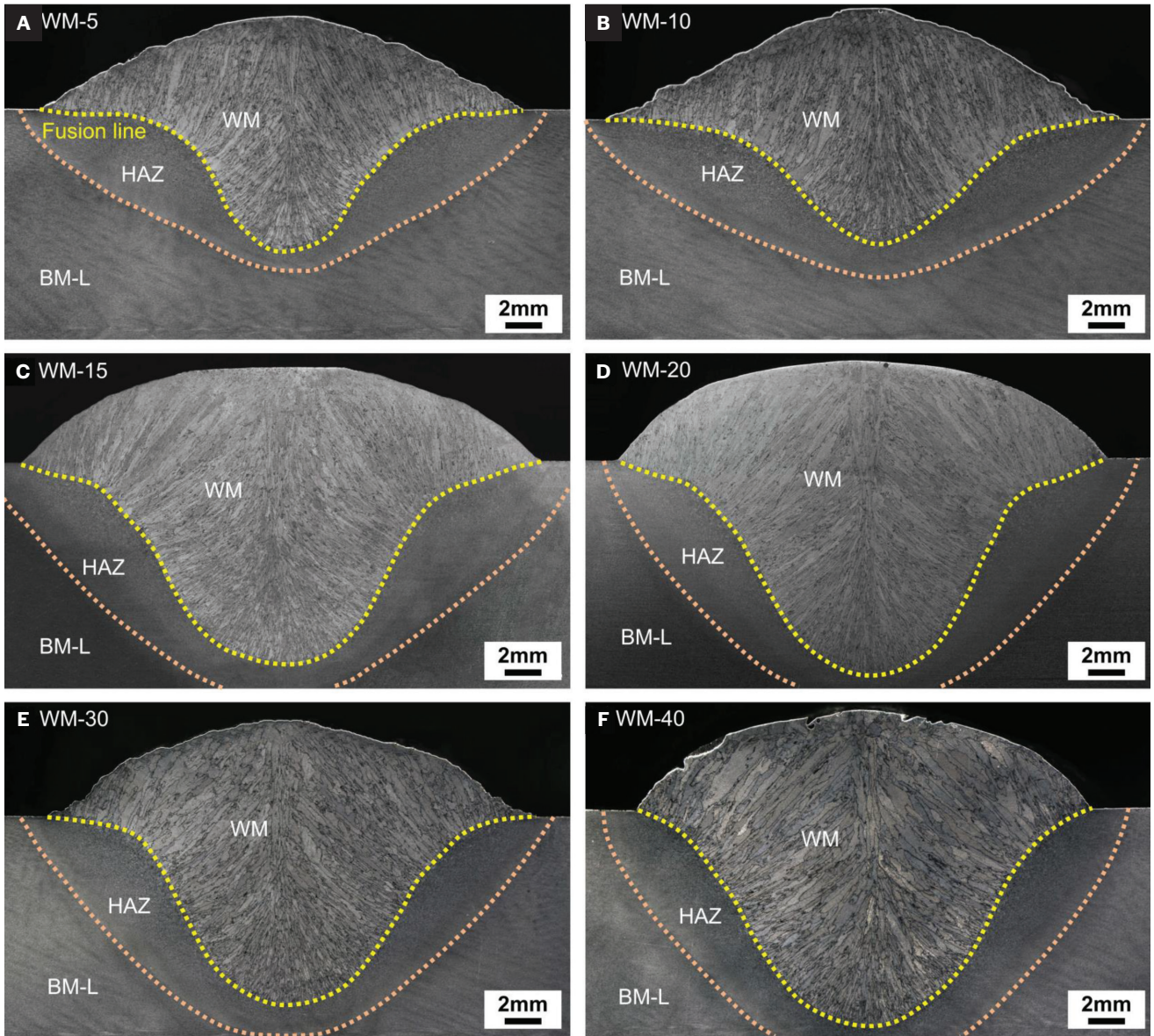
Fig. 1 — (A–F) Macro-morphology of the six WMs highlighting salient regions: WM, fusion line, HAZ, and base metal.

by a field-emission scanning electron microscope (FESEM, SU8010, Hitachi, Japan) under an acceleration voltage of 20.0 kV with a working distance of 15 mm, and at least 100 fields of view with a total area of approximately 0.230 mm^2 were examined for each WM.

Results

Figure 1 shows transverse macrographs of the six WMs, revealing defect-free welds. The columnar zone dominates the WMs in all samples, while the equiaxed zone is confined in the upper area. Weld bead shape parameters are found to change with flux compositions, as shown in Table 3. These phenomena resulted from the crucial role of flux composition in determining properties and weld bead shape (Refs. 27, 28). However, detailed discussion on the effect of flux com-

position on the weld bead shape is beyond the focus of this study, and it will be addressed in upcoming investigations.

For the sake of simplicity, we handpicked four representative WMs (WM-5, WM-20, WM-40, and WM-40H) for succinct discussion. Figures 2A–D show typical morphologies of CGs of the four WMs. Results indicated an anisotropic columnar morphology of prior γ grains. In WM-5, the WM exhibited a fine CG structure throughout. The average size was measured to be 102 μm. In WM-20, the CGs become larger in the middle and the top of the weld region, with an average width increase to 142 μm. In WM-40, substantial coarse CGs appeared in the entire WM. Frequently encountered coarse CGs with a short axis over 400 μm led to an average width increase of 250 μm. Overall, CG structure coarsened as SiO$_2$ content in the flux increased. However, when using BM-H, the WM exhibited fine CG structures. Figure 2D illustrates

Table 3 — Weld Bead Shape Parameters

WMs	w/mm	H_r/mm	D_p/mm	L_f/mm	S/mm²	θ/deg
WM-5	26.19	5.04	7.67	31.55	151.74	31.1
WM-10	28.05	6.07	6.61	32.48	164.83	26.3
WM-15	28.13	5.16	10.97	38.21	252.34	42.2
WM-20	26.64	5.41	11.57	36.87	252.54	48.2
WM-30	26.32	5.25	10.15	36.13	210.34	34.1
WM-40	24.55	5.43	11.82	36.57	253.08	54.9
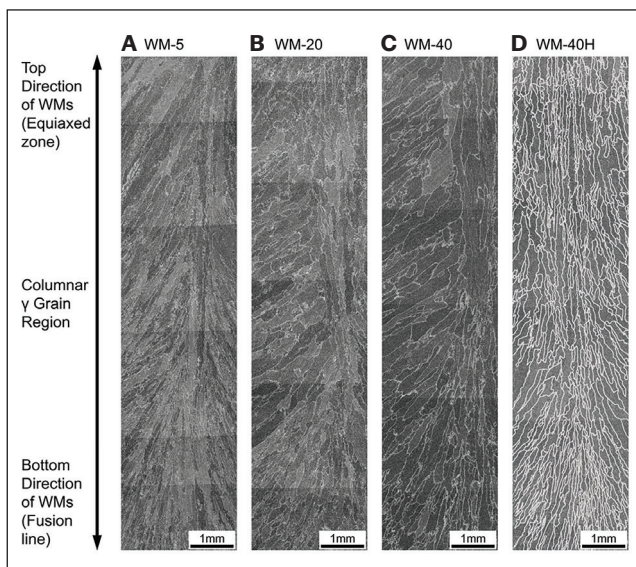
Fig. 2 — CG structures in: A — WM-5; B — WM-20; C — WM-40; D — WM-40H. In WM-5, WM-20, and WM-40, CG boundaries are visible due to proeutectoid α-ferrite along them. WM-40H has white lines as visual aids for CG boundaries.

Fig. 3 — Average CG size plotted against the distance from the fusion line for four WMs.

typical CGs in this WM. In WM-40H, a notable refined CG structure emerged across the WM, averaging 84 μm in width.

Figure 3 depicts detailed CG quantitative results in four WMs. At the fusion line, CGs in different weld samples exhibited substantially the same average size (~65 μm). Average CG size grew with distance from the fusion line in each WM; however, the growth rate (slope of the fitted line in Fig. 3) varied depending on the composition of the flux or the base metal used. For WM-5, there was a slight increase in average CG size from the fusion line (65 μm) to the top of the columnar zone (119 μm); for WM-20, such a growth rate of CG size increased, leading to a larger average CG size in the top of the columnar zone (200 μm); for WM-40, the CGs (300 μm) at the top exhibited a significant coarsening compared to the CGs close to the fusion line. However, when using BM-H, such a growing trend in WM-40H became flat similar to WM-5,
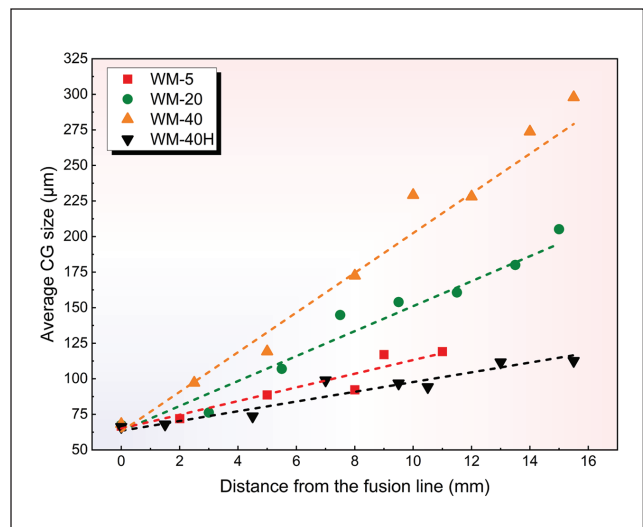
resulting in a smaller average size (113 μm) at the top. More detailed information regarding the macromorphology of WM-40H will be discussed later.

Si-Mn and Si-Mn-Al-(Ti) complex oxides with spherical shapes are dominant inclusions in EH36 steel WMs treated with CaF_2-SiO_2 fluxes, as recently reported (Ref. 23). Inclusion size, number density, and volume fraction in each WM are shown in Table 4. Calculations of mean spatial inclusion sizes $\bar{d}_v$ and the volume fraction f_v can be referred to elsewhere (Ref. 29). It clearly shows that the mean diameters $\bar{d}$ of the inclusions in all WMs were less than 1 μm, and the volume fraction f_v rose with the introduction of SiO_2 into the flux, which is consistent with previous findings (Ref. 23).
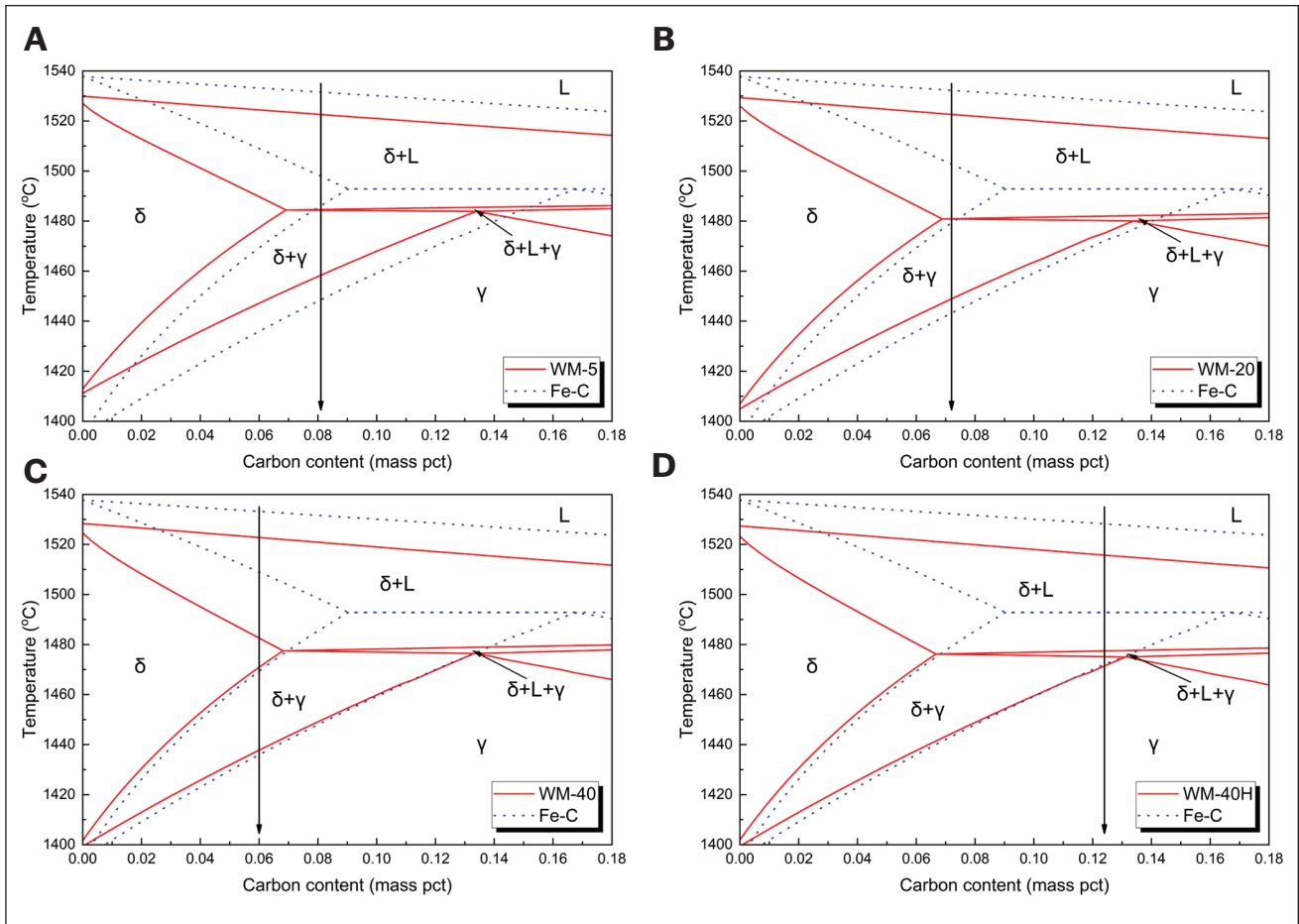
Fig. 4 — Pseudo-binary phase diagrams for: A — WM-5; B — WM-20; C — WM-40; D — WM-40H and the equilibrium Fe-C diagram. The vertical arrows indicate the equilibrium solidification path of corresponding WMs.

Discussion

Changes in Solidification Path Induced by Flux Composition Adjustment

The effect of SiO_2 on the element transfer behaviors has been well documented, as its addition enables Si and O transfer from the flux to the WM, which promotes the decarburization and Mn loss from the WMs (Refs. 21, 22). This element transfer behavior aligns with element content changes in Table 2.

Equilibrium solidification paths for various WMs are shown in Fig. 4 using pseudo-binary phase diagrams, which qualitatively illustrate the impact of major alloying elements (i.e., C, Si, and Mn) changes on solidification from a thermodynamic perspective. Equilibrium Fe-C diagram and pseudo-binary phase diagrams (Fe-C-Si-Mn) for WM-5, WM-20, WM-40, and WM-40H have been constructed using the FactSage 8.1 software (Phase Diagram Module) with SGTE and FactPS databases. With increasing SiO_2 content, the pseudo-binary phase diagram shifts towards the left and the lower temperature side, accompanied by a shrinkage of the δ phase region. The peritectic phase transition region changed into a triangular three-phase zone (Liquid $+δ+γ$), of which upper

and lower boundaries indicate peritectic start and end temperatures (Ref. 30).

In Figures 4A–C, decarburization from higher SiO_2 flux is evident, modifying the equilibrium solidification path (Ref. 21). For WM-5, of which the composition is in the hypo-peritectic range, the weld pool experiences solidification from liquid to δ, then peritectic transition occurs and the process of the transformation to γ coincides with the final solidification; with further cooling, all remaining δ transforms to γ. For WM-20, the C content gradually shifts to the left side, as evidenced in Fig. 4B. For WM-40, as the SiO_2 addition continuously increases, the C content moves to the left side further, which, however, alters the solidification mode of the weld pool into the non-peritectic one. After all liquid solidifies to δ, the transformation of δ to γ occurs without peritectic transition, as shown in Fig. 4C. Furthermore, Fig. 4D depicts the solidification path of WM-40H, which clearly shows that WM-40H solidifies following the peritectic transition.

Comparing the WMs' CG sizes (Fig. 3) with their equilibrium solidification paths (Fig. 4), fine CG structures are generally associated with peritectic processes. WM-5 and WM-40H, demonstrating typical peritectic behavior, exhibit fine CG structures.

Table 4 — Inclusion Size, Number Density, and Volume Fraction

WMs	d (μm)	$\bar{d}v$ (μm)	N (/mm²)	Nv (×10⁶/mm³)	fv (×10⁻² %)
WM-5	0.540	0.848	2960	3.49	11.14
WM-20	0.493	0.775	6320	8.15	19.88
WM-30	0.541	0.849	8757	10.31	33.08
WM-40	0.592	0.929	8513	9.16	38.51

Role of Inclusions on CG Size

O in WMs is another important element that can be notably changed by flux composition. As the weld pool solidifies, almost all O reacts with deoxidizing elements (dissolved Mn, Si, Al, Ti, etc.) to form oxide inclusions due to its low intrinsic solubility in solid Fe. Therefore, O content in WMs can be directly related to the inclusion volume fraction. It has been suggested (Refs. 12–14) that due to the pinning effect, an increase in inclusion content could lower the prior γ grain size. Since SAW is an O-gaining process and SiO_2-bearing flux promotes O transfer to the WMs (Refs. 17, 23), the impact of inclusions on CG size needs to be considered. Following the classical Zener theories, CG size D is calculated using Equation 1, relating inclusions diameter $\bar{d}_v$ and volume fraction f_v: (Refs. 13, 31).

$$D = 2\bar{d}v/3fv \qquad (1)$$

Figure 5 demonstrates the CG size and the inclusion volume fraction with SiO_2 content in the flux. Zener theory was used to make the calculations, and calculated CG sizes decreased from 507 to 161 μm with rising inclusion volume fraction. However, measured CG sizes showed an opposite trend, increasing from 102 ± 13 to 250 ± 63 μm with SiO_2 content rising from 5 to 40 mass-%. Calculated and measured sizes presented significant deviations, especially at 5 mass-% SiO_2 content. Similar phenomena were also reported in low-alloy steel welds deposited using both shielded metal arc welding (SMAW) (Ref. 5) and SAW (Ref. 2), where the variation of CG sizes was inconsistent with the expectations based on the increased pinning effect resulting from the rise of O content. Contrary to the results of Liu et al. (Ref. 13), these observations suggested limited pinning effect of inclusions on the formation of CG in as-deposited WMs.

Harrison et al. (Refs. 12, 31) reported dilatometry experiments, in which weld samples were reheated and held for 5 min at 1250°C for austenization. The observed equiaxed γ grain sizes exhibited a decreasing trend with increasing oxygen content. Ferrante et al. (Ref. 14) reported similar findings. The observations were further supported by comparing measured values to predictions derived from an extended form of Zener's equation. The results showed that the predicted values followed the experimental trend, indicating the pinning effect of inclusions. Nevertheless, such experiments, involving the migration of γ/γ boundaries during the coarsening of equiaxed γ grains under isothermal conditions, are quite different from
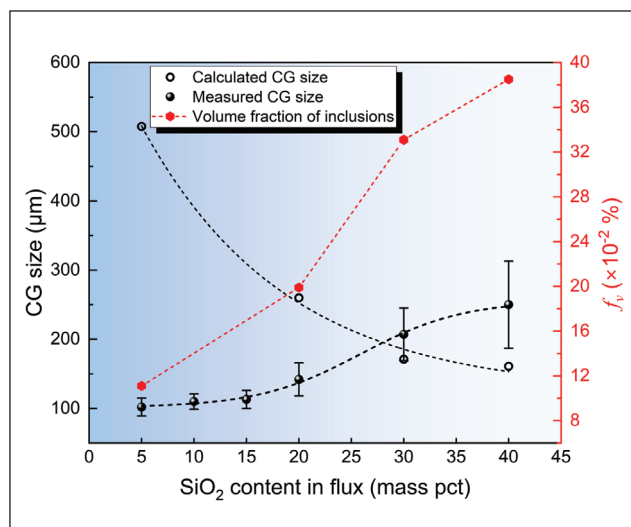

Fig. 5 — Comparison of CG size between calculated and measured, and the variation in inclusion volume fraction with SiO_2 content in the flux.

the anisotropic CG formation from δ or liquid phases during welding. The driving force for γ formation from δ depends on undercooling and is supposed to be appreciably greater than that needed for γ/γ boundary pinning (Ref. 2). Bhadeshia et al. (Ref. 2) proposed that inclusions formed in the weld pool were trapped and ultimately engulfed by the advancing δ/L interface without substantially affecting δ and/or ensuing γ grain growth during solidification. Considering that the effectiveness of inclusions as pinning phases depends on their size and volume fraction in relation to the grain size, inclusion pinning may be more significant in the case of reheated WMs than as-deposited WMs, where the γ grains form by a process of phase transition from the δ and/or liquid phases.

Effect of WM Macromorphology

WM macromorphology, another factor impacted by the flux composition, may influence the cooling rate and, thus, γ grain growth in the WM (Refs. 15, 16). As weld bead shapes change with added SiO_2 (Fig. 1), this could obscure explanations of the roles played by WM chemistries for CG structure changes. Therefore, it is necessary to evaluate the impact of WM macromorphology on CG structures. Basu et al. (Ref. 15)
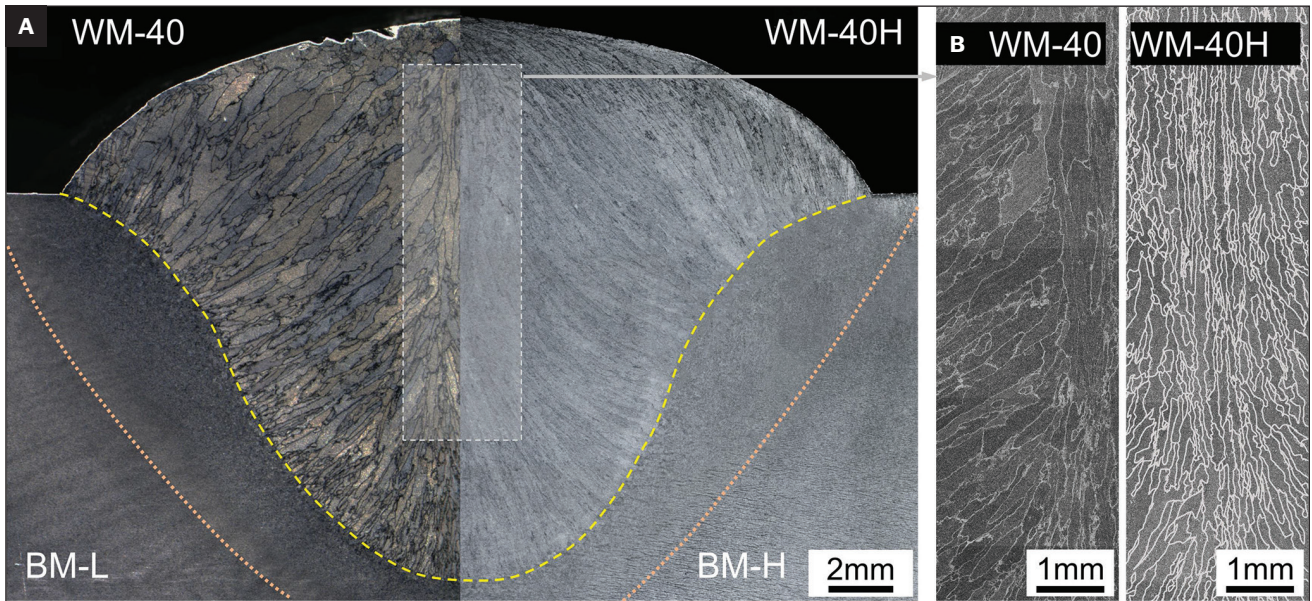
Fig. 6 — A — Transverse macrographs; B — CG structure of WM-40 and WM-40H.
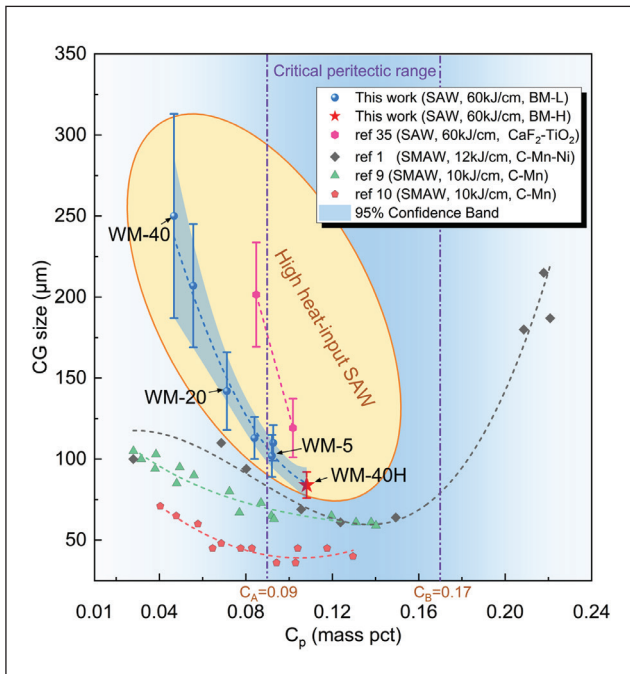

Fig. 7 — Chart of the relationship between CG size and Cp in the current work and those reported in the literature, including shielded metal arc welding (SMAW) for C-Mn-Ni welds reported by Zhang et al. (Ref. 1), C-Mn welds reported by Evans (Ref. 9) and Svensson et al. (Ref. 10), and SAW with CaF_2–TiO_2 flux for EH36 welds reported by Wu et al. (Ref. 35).

proposed a new parameter, NA/C1, (defined as the ratio of the weld bead area and fusion line length) to quantify the effect of submerged arc welded metal morphology on the cooling rate of WMs and found that the higher such parameter was, the larger prior γ grain size would be. Such a parameter may explain the relatively fine CG structure that appears in WM-5 (NA/C1 =

4.81 mm) compared with that of coarser grains appearing in WM-20 (NA/C1 = 6.85 mm) and WM-40 (NA/C1 = 6.92 mm). However, a subtle NA/C1 change in WM-20 and WM-40 does not seem to be a reason for the large CG size difference in Fig. 3. Therefore, the effect of WM macromorphology on CG size remains an open issue and requires further discussion.

Figure 6 shows the comparison of the transverse macrographs and CG structures between WM-40 and WM-40H. Figure 6A displays symmetrical WM shapes due to the same flux S-40 welding, as anticipated. The most-striking phenomenon is the formation of extremely fine CG structure in WM-40H, as shown in Fig. 6B, of which the average size is only 84 μm. In contrast, the CG size of WM-40 sharply increased to around three-fold that of WM-40H. The contrasting CG structures of WM-40 and WM-40H strongly indicate that the variation in WM chemical compositions, rather than that in WM macromorphology, is the dominant factor altering the CG structure.

Variation in CG size with Equivalent Carbon Content

In continuous casting, the prevailing approach to assess the influence of individual alloying elements on the solidification of certain steel grades is by determining the equivalent carbon content (Cp) (Ref. 32). Cp can be calculated by summing the composition of different alloying elements multiplied by dimensionless weighting coefficients, where austenite formers, such as Mn and Ni, are positively weighted and ferrite formers, such as Si, Cr, and Mo, are negatively weighted (Ref. 32). Equation 2 was proposed by Wolf (Ref. 33) for low-carbon low-alloy steel to predict peritectic behavior in steel. If the calculated Cp falls within a critical range of 0.09 (C_A) to 0.17 (C_B) mass-% C, the steel is classified as peritectic (Refs. 32, 34).

$$Cp = [C] + 0.02[Mn] + 0.04[Ni] - 0.1[Si] - 0.04[Cr] - 0.1[Mo] \qquad (2)$$

Figure 7 shows the variation in CG size with *Cp*. It demonstrates that as *Cp* increased, CG size was depressed in the present study. WMs with compositions within the critical peritectic range exhibited finer grain structures compared to non-peritectic ones. Specifically, the CG size of WM-40H, using hyper-peritectic steel BM-H, was dramatically small. This highly suggests the significant importance of solidification modes. Moreover, when comparing the CG size with those reported under various welding conditions, it was shown that alterations in CG size with *Cp* in other investigations followed a similar trend. According to Zhang et al. (Ref. 1), CG size initially decreases with increasing Ni equivalent then coarsens. WMs with the smallest CGs generally possess a Ni equivalent within the peritectic range, as indicated by the gray dashed line in Fig. 7 (*Cp* is employed for calculation, and the trend in CG size remains consistent). They proposed that the variation in CG size encountered in WMs could be attributed to differences in solidification modes. For WMs with compositions falling within the peritectic range, a series of phase transformations take place. These include L→δ solidification, L + δ→γ peritectic reaction, and δ→γ and L→γ peritectic transformation. These transformations occur sequentially at different moments and various locations within the weld pool, which potentially disrupts the continuous growth of γ grains, resulting in the formation of finer CGs (Ref. 1). Moreover, given that γ, undergoing peritectic reaction, nucleates at the liquid/δ interface, the remaining liquid phase amidst δ dendrites will serve as a pinning phase for γ grain growth. This may inhibit the coarsening of γ in the lateral direction (Refs. 36–38).

Furthermore, Fig. 7 also indicates the effect of welding conditions. The CG structure, as expected, coarsens with the increase of welding heat input, which is attributed to the prolonged cooling undergoing in these high heat input WMs (Ref. 39). Notably, the influence of welding heat input on CG size is primarily evident in the non-peritectic range. As *Cp* diminishes, disparities in CG size under different heat inputs become increasingly pronounced.

As described above, CG structure can be tailored by tuning flux composition. According to *Cp* calculation, it is postulated that incorporating certain oxides like SiO_2, TiO_2, Cr_2O_3, Al_2O_3, et al., which promote decarburization and encourage the transfer of ferrite-forming elements into low-carbon low-alloy steel WMs, may contribute to coarsening the CG structure. This hypothesis has been preliminarily supported by observing the change in CG size during SAW with CaF_2-TiO_2 fluxes (Fig. 7) (Ref. 35). Additionally, it is important to note that C and other alloying elements in the final WMs originate from a combination of the welding wire, base metal, and flux (Ref. 40). To ultimately achieve the desired CG structure through flux optimization, careful consideration should also be given to the composition of the welding wire and base metal.

Summary

We have investigated the variation in CG size contingent upon SiO_2 content using SAW on EH36 shipbuilding steel with CaF_2-SiO_2 fluxes. Specifically, factors influencing CG size were explored because they may contribute to the optimization of the welding flux design for the CG structure. Key findings are outlined below:

1. In EH36 steel subjected to single-pass tandem SAW with CaF_2-SiO_2 fluxes, the as-deposited metal is primarily comprised of CGs. Incorporating SiO_2 at levels from 5 to 40 mass-% increases CG size by a factor of nearly 2.5, coincidental with a transition in equilibrium solidification mode from peritectic to primary δ solidification.

2. As the equivalent carbon content of the WMs rises from 0.047 to 0.108 mass-%, there is a steady reduction in CG size. The smallest CGs are observed in WMs with equivalent carbon content within the peritectic range (0.09 to 0.17 mass-%) in the current work and those reported in the literature.

3. The classical Zener theory was employed to predict the CG size in WMs; however, it demonstrates a contrasting trend compared to the measured ones as SiO_2 content increases. Therefore, a sizable population of inclusions gained during SAW shall not be the dominant factor influencing CG size in the current work.

4. Despite sharing similar macro-morphologies, CGs formed by primary δ solidification based on the equivalent carbon content during welding of low-C base metal are approximately three times greater compared to those formed by peritectic solidification when welding high-C base metal using the same flux CaF_2-40SiO_2.

Acknowledgments

Disclosure Statement

No potential conflict of interest was reported by the author(s).

References

1. Zhang, Z., and Farrar, R. A. 1995. Columnar grain development in C-Mn-Ni low-alloy weld metals and the influence of nickel. *Journal of Materials Science* 30(22): 5581–5588. DOI: 10.1007/BF00356690

2. Bhadeshia, H. K. D. H., Svensson, L. E., and Gretoft, B. 1986. The austenite grain structure of low-alloy steel weld deposits. *Journal of Materials Science* 21(11): 3947–3951. DOI: 10.1007/BF02431634

3. Bhadeshia, H. K. D. H. 2008. Application of phase transformation theory to welding. *POSCO Lectures*. Portland. 109–144.

4. Evans, G. M., and Bailey, N. 1997. *Metallurgy of Basic Weld Metal*. Cambridge: Woodhead Publishing.

5. Bhadeshia, H. K. D. H., Svensson, L. E., and Gretoft, B. 1985. A model for the development of microstructure in low-alloy steel (Fe-Mn-Si-C) weld deposits. *Acta Metallurgica* 33(7): 1271–1283. DOI: 10.1016/0001-6160(85)90238-X

6. Farrar, R. A., Zhang, Z., Bannister, S. R., and Barritte, G. S. 1993. The effect of prior austenite grain size on the transformation behaviour of C-Mn-Ni weld metal. *Journal of Materials Science* 28(5): 1385–1390. DOI: 10.1007/BF01191982

7. Thewlis, G. 1994. Transformation kinetics of ferrous weld metals. *Materials Science and Technology* 10(2): 110–125. DOI: 10.1179/mst.1994.10.2.110

8. Thewlis, G., Whiteman, J. A., and Senogles, D.J. 1997. Dynamics of austenite to ferrite phase transformation in ferrous weld metals. *Materials Science and Technology* 13(3): 257–274. DOI: 10.1179/mst.1997.13.3.257

9. Evans, G. M. 1983. The effect of carbon on the microstructure and properties of all-weld-metal deposits. *Welding Journal* 62(11): 313-s to 320-s.

10. Svensson, L. E., and Gretoft, B. 1990. Microstructure and impact toughness of C-Mn weld metals. *Welding Journal* 69(12): 454-s to 461-s.

11. Zhang, Z., and Farrar, R. A. 1997. Influence of Mn and Ni on the microstructure and toughness of C-Mn-Ni weld metals. *Welding Journal* 76(12): 183-s to 196-s.

12. Harrison, P. L., and Farrar, R. A. 1981. Influence of oxygen-rich inclusions on the γ→α phase transformation in high-strength low-alloy (HSLA) steel weld metals. *Journal of Materials Science* 16(8): 2218–2226. DOI:10.1007/BF00542384

13. Liu, S., and Olson, D. L. 1986. The role of inclusions in controlling HSLA steel weld microstructures. *Welding Journal* 2(6): 139-s to 149-s.

14. Ferrante, M., and Farrar, R. A. 1982. The role of oxygen rich inclusions in determining the microstructure of weld metal deposits. *Journal of Materials Science* 17(11): 3293–3298. DOI: 10.1007/BF01203498

15. Basu, B., and Raman, R. 2002. Microstructural variations in a high-strength structural steel weld under isoheat input conditions. *Welding Journal* 81(11): 239-s to 248-s.

16. Kiran, D. V., Cho, D. W., Lee, H. K., Kang, C. Y., and Na, S. J. 2015. A study on the quality of two-wire tandem submerged arc welds under iso-heat input conditions. *International Journal of Advanced Manufacturing Technology* 78: 53–62. DOI: 10.1007/s00170-014-6644-3

17. Wang, C., and Zhang, J. 2021. Fine-tuning weld metal compositions via flux optimization in submerged arc welding: an overview. *Acta Metallurgica Sinica* 57(9): 1126–1140. DOI: 10.11900/0412.1961.2021.00148

18. Chai, C. S. 1980. Slag-metal reactions during flux shielded arc welding. PhD diss. Massachusetts Institute of Technology, Cambridge, Mass.

19. Ferrera, K. P., and Olson, D. L. 1975. Performance of the MnO-SiO2-CaO system as a welding flux. *Welding Journal* 54(7): 221-s to 215-s.

20. Olson, D. L., Dixon, R., and Liby, A. L. 1990. *Welding: theory and practice*. Amsterdam: North-Holland.

21. Zhang, J., Coetsee, T., Dong, H., and Wang, C. 2020. Elucidating the roles of SiO$_2$ and MnO upon decarburization during submerged arc welding: a thermodynamic study into EH36 shipbuilding steel. *Metallurgical and Materials Transactions B* 51(4): 1805–1812. DOI: 10.1007/s11663-020-01869-x

22. Zhang, J., Coetsee, T., and Wang, C. 2020. Element transfer behaviors of fused CaF$_2$-SiO$_2$ fluxes subject to high heat input submerged arc welding. *Metallurgical and Materials Transactions B* 51(1): 16–21. DOI: 10.1007/s11663-019-01753-3

23. Han, C., Zhong, M., Kaldre, I., Zhao, H., Zhao, P., and Wang, C. 2023. Role of SiO$_2$ upon weld metal inclusion characteristics in EH36 shipbuilding steels treated by CaF$_2$-SiO$_2$ fluxes. *Metallurgical and Materials Transactions B* 54(3): 989–995. DOI: 10.1007/s11663-023-02781-w

24. Wesley, W., and Liu, S. 1993. Nature and behavior of fluxes used for welding. *ASM Handbook: Welding Brazing and Soldering*, 43–54.

25. Allibert, M., Gaye, H., Geiseler, J., Janke, D., and Keene, B. J. 1995. *Slag Atlas*. Düsseldorf, Germany: Verlag Stahleisen GmbH.

26. Geels, K., Fowler, D. B., Kopp, W. U., and Ruckert, M. 2007. Metallographic and materialographic specimen preparation, light microscopy, image analysis and hardness testing. *Materials Science, Engineering* 565–576. West Conshohocken, Penn.: ASTM International.

27. Schwemmer, D. D., Olson, D. L., and Williamson, D. L. 1979. The relationship of weld penetration to the welding flux. *Welding Journal* 58: 153-s to 160-s.

28. Wang, Z., Li, Z., Zhong, M., Li, Z., and Wang, C. 2023. Elucidating the effect of Al$_2$O$_3$/SiO$_2$ mass ratio upon SiO$_2$-MnO-CaF$_2$-Al$_2$O$_3$-based welding fluxes: Structural analysis and thermodynamic evaluation. *Journal of Non-Crystalline Solids* 601: 122071. DOI: 10.1016/j.jnoncrysol.2022.122071

29. Sakata, K., and Suito, H. 1999. Dispersion of fine primary inclusions of MgO and ZrO$_2$ in Fe-10 mass pct Ni alloy and the solidification structure. *Metallurgical and Materials Transactions B: Process Metallurgy and Materials Processing Science* 30(6): 1053–1063. DOI: 10.1007/s11663-999-0111-9

30. Liu, T., Long, M., Chen, D., Huang, Y., Yang, J., Duan, H., Gui, L., and Xu, P. 2020. Investigation of the peritectic phase transition in a commercial peritectic steel under different cooling rates using in situ observation. *Metallurgical and Materials Transactions B* 51(1): 338–352. DOI: 10.1007/s11663-019-01758-y

31. Harrison, P. L. 1981. Continuous cooling transformation kinetics and microstructure of mild and low-alloy steel weld metals. Doctoral diss., University of Southampton,

32. Presoly, P., Pierer, R., and Bernhard, C. 2013. Identification of defect prone peritectic steel grades by analyzing high-temperature phase transformations. *Metallurgical and Materials Transactions A* 44(12): 5377–5388. DOI: 10.1007/s11661-013-1671-5

33. Wolf, M. M. 1997. *Continuous casting: Initial solidification & strand surface quality of peritectic steels*, 61–65. Iron and Steel Society of AIME.

34. Azizi, G., Thomas, B. G., and Asle Zaeem, M. 2020. Review of peritectic solidification mechanisms and effects in steel casting. *Metallurgical and Materials Transactions B* 51(5): 1875–1903. DOI: 10.1007/s11663-020-01942-5

35. Wu, Y., Yuan, X., Kaldre, I., Zhong, M., Wang, Z., and Wang, C. 2023. TiO$_2$-assisted microstructural variations in the weld metal of EH36 shipbuilding steel subject to high heat input submerged arc welding. *Metallurgical and Materials Transactions B* 54(1): 50–55. DOI: 10.1007/s11663-022-02697-x

36. Pottore, N. S., Garcia, C.I., and DeArdo, A. J. 1991. Interrupted and isothermal solidification studies of low and medium carbon steels. *Metallurgical Transactions A* 22(8): 1871–1880. DOI: 10.1007/BF02646512

37. Tsuchiya, S., Ohno, M., Matsuura, K., and Isobe, K. 2011. Formation mechanism of coarse columnar γ grains in as-cast hyper-peritectic carbon steels. *Acta Materialia* 59(9): 3334–3342. DOI: 10.1016/j.actamat.2011.02.007

38. Ohno, M., Tsuchiya, S., and Matsuura, K. 2011. Formation conditions of coarse columnar austenite grain structure in peritectic carbon steels by the discontinuous grain growth mechanism. *Acta Materialia* 59(14): 5700–5709. DOI: 10.1016/j.actamat.2011.05.045

39. Grong, O. 1997. *Metallurgical Modelling of Welding*, 221–296. Norway: The Institute of Materials.

40. Natalie, C., Olson, D. L., and Blander, M. 1986. Physical and chemical behavior of welding fluxes. *Annual Review of Materials Science* 16: 389–413.

CHAO HAN, MING ZHONG, PENG ZUO, and **CONG WANG** (*wangc@smm.neu.edu.cn*) are with Key Laboratory for Ecological Metallurgy of Multimetallic Mineral (Ministry of Education), Northeastern University, Shenyang, China. They are also with the School of Metallurgy, Northeastern University, Shenyang, China.